Environmental Fluid Mechanics **2:** 241–263, 2002.

Experimental Study of Gas-Liquid Interfacial Properties in a Stepped Cascade Flow

HUBERT CHANSON* and LUKE TOOMBES
Department of Civil Engineering, The University of Queensland, Brisbane QLD 4072, Australia

Received 12 November 2001; accepted in revised form 26 February 2002

Abstract. Gas-liquid interface measurements were conducted in a strongly turbulent free-surface flow (i.e., stepped cascade). Local void fractions, bubble count rates, bubble size distributions and gas-liquid interface areas were measured simultaneously in the air-water flow region using resistivity probes. The results highlight the air-water mass transfer potential of a stepped cascade with measured specific interface area over 650 m^{-1} and depth-average specific area up to 310 m^{-1}. A comparison between single-tip and double-tip resistivity probes suggests that simple robust single-tip probes may provide accurate, although conservative, gas-liquid interfacial properties. The latter device may be used in the field and in prototype plants.

Notation

a	=	specific interface area (m^{-1});
a_{mean}	=	depth-average specific interface area (m^{-1}): $a_{mean} = \frac{1}{Y_{90}} \int_0^{Y_{90}} (1 - C)\, dy$;
C	=	local void fraction;
C_{gas}	=	dissolved gas concentration (kg m^{-3});
C_{mean}	=	depth-average mean air concentration defined as: $C_{mean} = 1 - d/Y_{90}$;
C_s	=	saturation concentration (kg m^{-3});
D'	=	dimensionless air bubble diffusivity (defined by [1]);
d	=	equivalent clear-water flow depth (m): $d = \int_0^{Y_{90}} (1 - C)\, dy$;
d_{ab}	=	air bubble diameter (m);
d_c	=	critical flow depth (m); for a rectangular channel: $d_c = \sqrt[3]{q_w^2/g}$;
F	=	air bubble count rate (Hz);
F_{max}	=	maximum bubble count rate (Hz), often observed for $C = 50\%$;
g	=	gravity acceleration (m s^{-2});
h	=	step height (m);
K_L	=	liquid film coefficient (m s^{-1});
K′	=	integration constant defined as: $K' = \tanh^{-1}(\sqrt{0.1}) + (2D')^{-1}$ [1];
L	=	chute length (m);
N	=	velocity distribution exponent;

*Corresponding author, E-mail: h.chanson@mailbox.uq.edu.au

Q_w	=	water discharge (m^3 s^{-1});
q_w	=	water discharge per unit width (m^2 s^{-1});
t	=	time (s);
V	=	local velocity (m s^{-1});
V_c	=	critical flow velocity (m s^{-1}); for a rectangular channel: $V_c = \sqrt[3]{q_w g}$
V_{max}	=	maximum air-water velocity (m s^{-1});
V_{90}	=	characteristic air-water velocity (m s^{-1}) where C = 90%;
W	=	channel width (m);
x	=	longitudinal distance (m) measured along the flow direction (i.e., parallel to the pseudo-bottom formed by the step edges);
y	=	distance (m) normal to the pseudo-bottom formed by the step edges;
Y_{90}	=	characteristic distance (m) where $C = 0.90$;
Y_{98}	=	characteristic distance (m) where $C = 0.98$;
α	=	slope of pseudo-bottom by the step edges;
$\emptyset$	=	diameter (m).

Key words: air-water interface, experiments, mass transfer, stepped cascade

1. Introduction

Aeration enhancement by macro-roughness is well-known in water treatment and one form is the aeration cascade. In Chicago, five re-aeration cascades were built to re-oxygenate the depleted waters of the Calumet waterway. In operation, their aeration efficiency corrected to a temperature of 15 °C is nearly 95% [2]. Similarly in-stream cascades have been built along polluted and eutrophic streams. Stepped weirs are designed downstream of large dams to control the quality of water releases (e.g., nitrogen supersaturation effect). Despite the associated hydropower loss, a two-step re-aeration cascade was added downstream of the Petit-Saut dam in French Guyana to treat turbined waters which had unacceptably high methane content [3]. Re-aeration cascades are also used in water treatment for re-oxygenation, denitrification or VOC removals. The Montferland plant in the Netherlands was designed to remove nitrate from ground water by sulphur/limestone denitrification. It includes an aeration cascade to re-oxygenate depleted waters at the end of the process [4]. Overall stepped cascades are very efficient because of the strong turbulent mixing associated with substantial air entrainment.

Despite numerous industrial applications, little is known on the gas-liquid interfacial properties of stepped cascade flows (e.g., [5]). Basic experimental investigations of air-water interfacial properties require the measurements of void concentration, air-water velocity, bubble and droplet sizes, and air-water interface areas. In an air-water mixture, classical measurement devices (e.g., Pitot tube, LDA velocimeters) may lead to inaccurate data. Some measurement systems were developed specifically for gas-liquid flows: e.g., resistivity probes, optical probes,

conical hot-film probes, Fibre Phase Doppler Anemometer (FPDA) and LDA/PDA systems although some systems have limitations in terms of void fraction and velocity ranges. Authoritative reviews on two-phase flow measurement systems include Jones and Delhaye [6], Cartellier and Achard [7], Bachalo [8] and Chanson [1].

In stepped chute flows, resistivity and optical probes were used recently to record void fraction and velocity distributions with void fractions ranging from 10 to 95% (e.g., [9, 10]). The technique has however not been extended yet to interfacial properties. The present study describes an experimental study of air-water interfacial properties in a stepped cascade. Conventional resistivity probes were used to provide gas-liquid interfacial properties and comparative performances between two sensor sizes are described. The results are applicable in the field and in industrial plants where sturdy thick probe sensors are more appropriate, yet less sensitive to the smallest bubbles.

2. Experiments

Experiments were conducted at the University of Queensland in a 2.7 m long, 1 m wide chute (21.8° slope) with flow rates ranging from 45 to 200 L s^{-1}. The chute consists of a broad-crest followed by 9 identical steps ($h = 0.1$ m) (Figure 1). The cascade geometry and range of flow rates were selected to be nearly full-scale and to minimise potential scale effects. Waters are supplied by a pump controlled with adjustable frequency AC motor drive enabling an accurate discharge adjustment in a closed-circuit system. The flow rates are measured from the upstream head above crest with an accuracy of about 2% [11, 12].

Clear-water flow depths and velocities were measured with a point gauge and a Prandtl–Pitot tube ($\emptyset = 3.3$ mm) respectively. The air-water flow properties were measured using a single-tip resistivity probe ($\emptyset = 0.35$ mm) and a double-tip resistivity probe [13, 14]. In the latter, the two tips were aligned in the direction of the flow (Figure 2). The probe tips were identical with an internal electrode ($\emptyset = 25$ μm, Pt) and an external concentric stainless steel electrode of 200 μm diameter. The probe was built with two trailing tips. The outer trailing tip was designed to provide a response, should a wake form behind the leading tip and affect the main trailing tip (e.g., [15, 16]). During the present study, the outer trailing tip was not needed.

Both resistivity probes were excited by an air bubble detector (AS25240). The electronics was designed with a response time less than 10 μs and was calibrated with a square wave generator. The single-tip probe signal was scanned at 5 kHz for 180 s while the double-tip resistivity probe signal was scanned at 20 kHz for 20 s (per channel).

The translation of the probes in the direction normal to the pseudo-bottom formed by the step edges was controlled by a fine adjustment travelling mechanism connected to a Mitutoyo™ digimatic scale unit. The error on the normal position

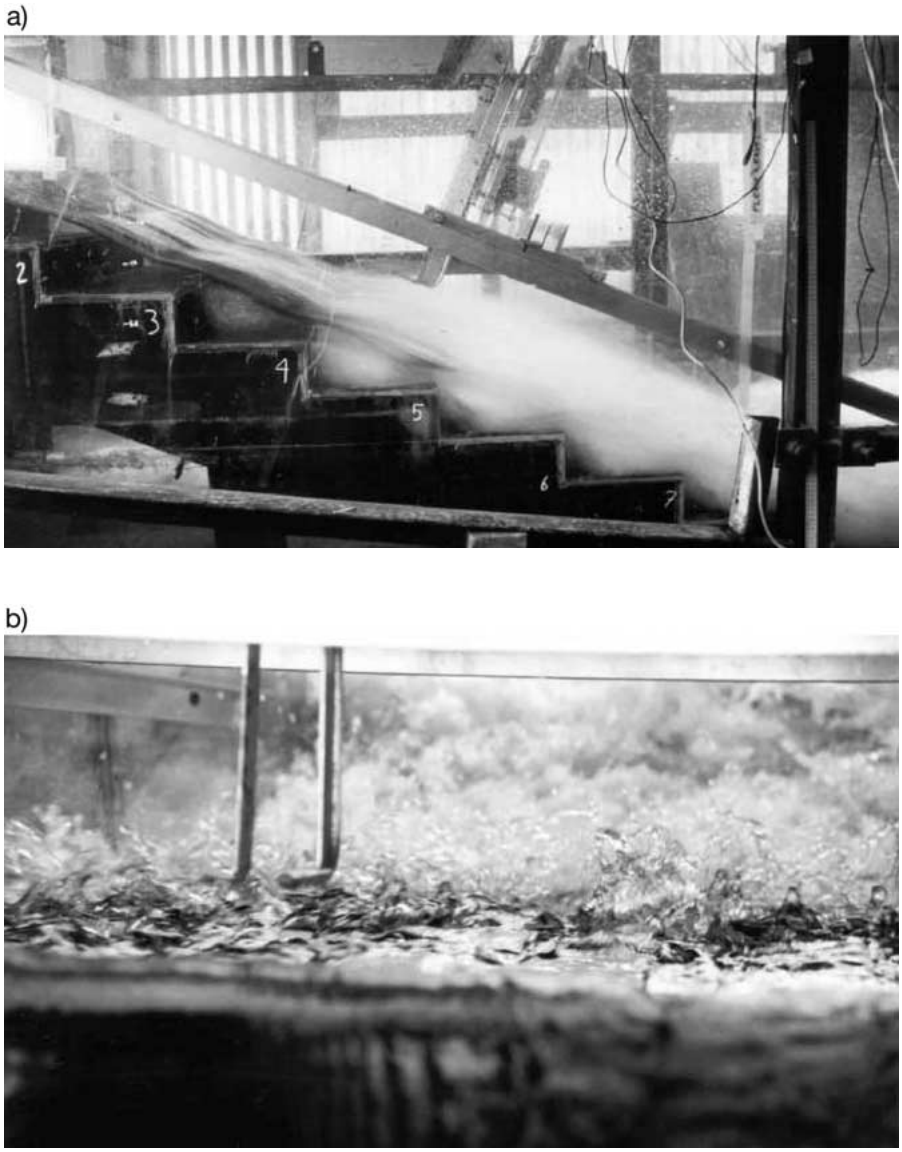

Figure 1. Experimental stepped cascade. (a) Experiment No. 2: $q_w = 0.114$ m^3 s^{-1} (skimming flow). Side view (low shutter speed). (b) Experiment No. 1: $q_w = 0.18$ m^2 s^{-1} (skimming flow). View from upstream looking at the spray and splashing with the trolley and probe supports in background (1/2000 s shutter speed). (c) Experiment No. 3: $q_w = 0.058$ m^2 s^{-1} (transition flow). Detailed flow pattern at step edges 4, 5 and 6 (1/2000 s shutter speed). (d) Definition sketch.

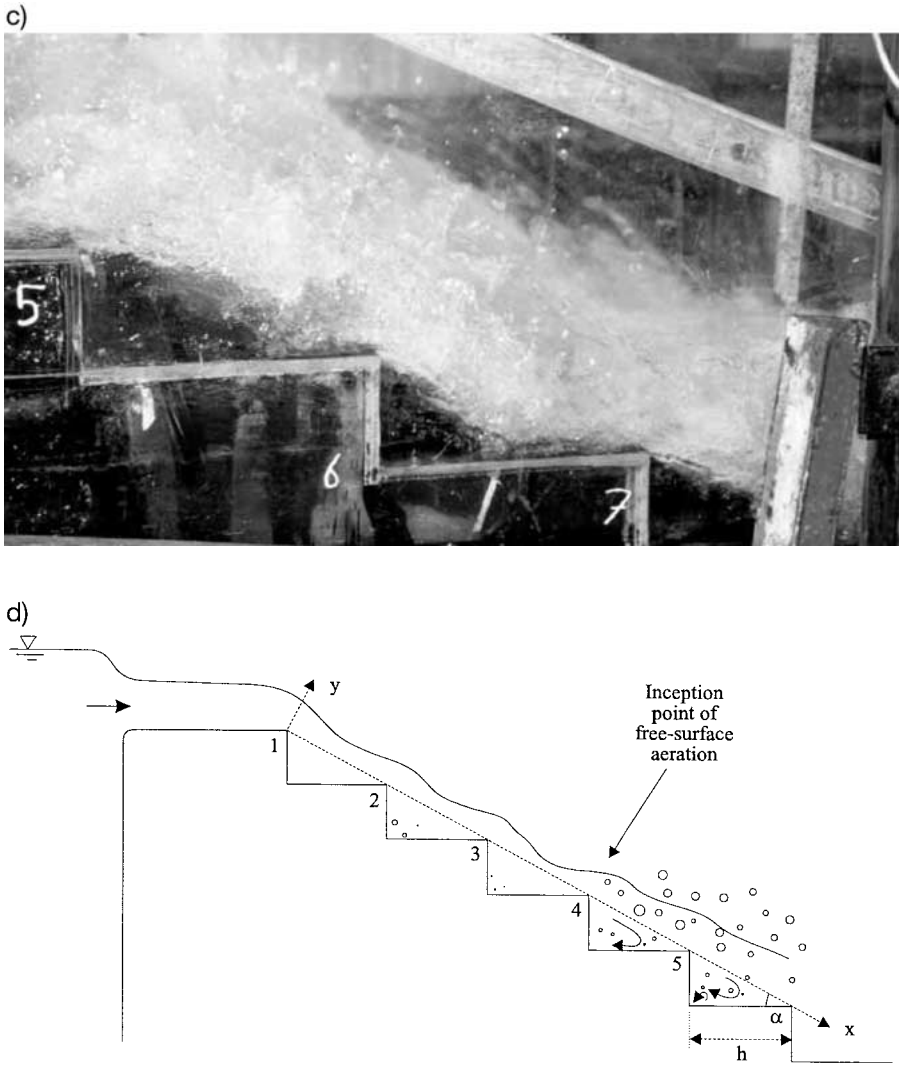

Figure 1. Continued.

of the probe was less than 0.2 mm. The accuracy on the longitudinal position of the probe was estimated as $\Delta x < +/- 0.5$ cm. The accuracy on the transverse position of the probe was less than 1 cm. Flow visualisations were conducted with a digital video-camera Sony™DV-CCD DCR-TRV900 (speed: 25 fra s^{-1}, shutter: 1/4 to 1/10 000 s) and high-speed still photographs.

2.1. FLOW CONDITIONS

A stepped cascade flow is characterised by a succession of free-falling nappes (i.e., nappe flow) at low flow rates. At large flow rates with identical chute geome-

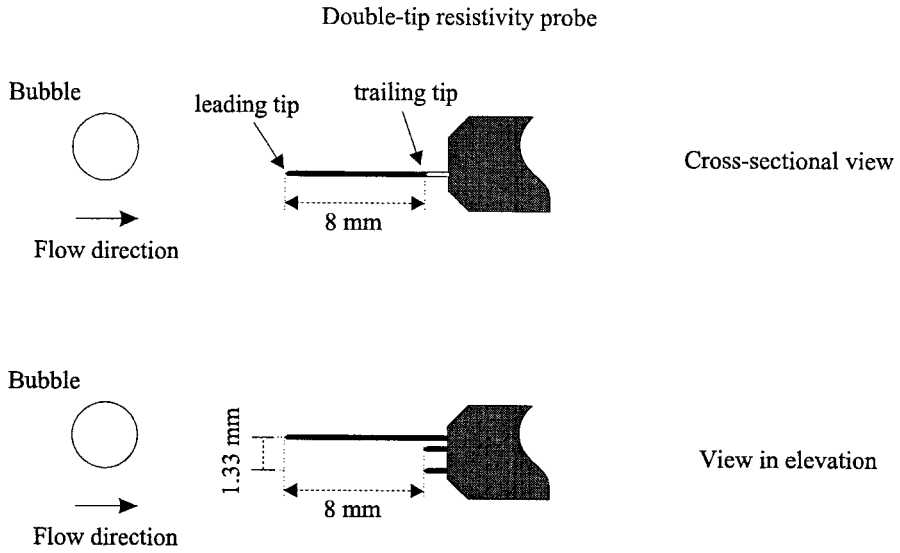

Figure 2. Sketch of the resistivity probe designs.

try (step height, mean slope), the water skims over the pseudo-invert formed by the step edges (i.e., skimming flow). For an observer on the chute bank, a skimming flow has the same appearance as a smooth-invert chute flow. For a range of flow rates in between, a transition flow pattern is observed. It is characterised by significant splashing and flow deflections at some steps.

The experimental chute was designed to operate either with nappe flow, transition flow or skimming flow. Nappe flow was observed for $d_c/h < 0.52$ where d_c is the critical flow depth and h is the step height; skimming flow was observed for $d_c/h > 1.0$ with a transition flow pattern for $0.52 < d_c/h < 1.0$. The present series of investigations were conducted with two flow patterns: transition and skimming flow regimes. Detailed measurements were performed with both resistivity probes for identical flow conditions (Table I). The probe tips were located on the channel centreline at step edges for all flows, and additional measurements were conducted between (half-way) edges in skimming flows with the double-tip probe. Further details on the experiments and results are reported in Chanson and Toombes [17].

2.2. DATA ANALYSIS

The analysis of single-tip resistivity probe data provided point measurements of the void fraction C (i.e., air concentration) and bubble count rate F defined as the number of bubbles or droplets impacting a probe tip per second. The double-tip conductivity probe measurements provided additionally the mean air-water interface velocity V, chord length distributions and air-water interface area at various positions within a cross-section.

Table I. Detailed investigations of comparative performances of single-tip and double-tip resistivity probe.

Ref.	α	h	q_w	d_c/h	Remarks
	deg.	m	$m^2\ s^{-1}$		
(1)	(2)	(3)	(4)	(5)	(6)
UQ	21.8	0.10			Stepped cascade: $L = 2.7$, $W = 1$ m. Smooth sidewall convergent (4.8:1) followed by broad-crest. Low upstream turbulence. Nine flat horizontal steps.
Exp. 1			0.182	1.5	Skimming flow. Inception of free-surface aeration upstream of 6th step edge. Runs Q23 and Q5.
Exp. 2			0.114	1.1	Skimming flow. Inception of free-surface aeration upstream of 5th step edge. Run Q21 and Q9.
Exp. 3			0.058	0.7	Transition flow. Inception of free-surface aeration upstream of 3rd step edge. Runs Q14 and Q22.

Note : α – slope of the pseudo-bottom formed by the step edges.

Measurements of air-water interface area derive from the basic air-water flow properties. In monosize bubbly flows, the air-water specific interface area[1] may be estimated from the air bubble size:

$$a = 6\frac{C}{d_{ab}}, \tag{1}$$

where C is the void fraction and d_{ab} is the bubble diameter.[2] For a non-constant bubble size distribution, the local specific interface area equals:

$$a = \int_0^{+\infty} 6\Pr(d_{ab})\frac{C}{d_{ab}}d(d_{ab}), \tag{2}$$

where $\Pr(d_{ab})$ is the probability of bubble size d_{ab}. Experimental measurements with intrusive probes (e.g., resistivity, optical fibre) do not provide bubble diameters but chord length and bubble count data. For any bubble shape, bubble size distribution and chord length distribution, the mean chord length size[3] equals

[1] That is, the air-water interface area per unit volume of air and water.

[2] In a monosize droplet spray, the interfacial area equals $6(1 - C)/d_w$ where d_w is the droplet size.

[3] That is, the number mean size.

$C\ V/F$, where V is the local air-water velocity and F is the bubble count. The specific air-water interface area derives from the mass conservation for air:

$$a = \frac{4\ F}{V}. \tag{3}$$

The derivation of (3) is simple for spherical particles. It may be extended to ellipsoidal particles following the method of Clark and Turton [18] (also [19]). Equation (3) is basically valid in the bubbly flow region ($C < 0.3$) and in the spray ($C > 0.7$). For intermediate air contents ($0.3 < C < 0.7$), the flow structure is more complex and the result is not the true specific interface area. Equation (3) becomes proportional to the number of air-water interfaces per unit length of air-water mixture (i.e. $a \propto 2\ F/V$) which is an interfacial characteristics. Equation (3) was applied for $0 < C < 95\%$ for consistency of the results.

The data accuracy is typically $\Delta C/C < 2\%$ and $\Delta V/V < 5$ to 10% for void fractions between 3 to 95% and mean velocity larger than 0.5 m s^{-1}. The smallest detectable chord length size is about 0.35 mm with the single-tip probe and 0.05 mm (i.e., 50 μm) with the double-tip probe for the observed velocities (i.e., $V \sim 1$ to 3.5 m s^{-1}) and selected scanning rate (20 kHz). The accuracy on the bubble count rate is a function of the bubble size distributions. In the present study, the mean bubble size was about two orders of magnitude greater than the double-tip probe sensor and the accuracy on bubble count rate is about $\Delta F/F < 3$ to 5% (double-tip sensor), yielding errors on the specific interface area less than 10 to 15%.

3. Void Fraction Distributions

In transition and skimming flows, the free-surface is clear and transparent on the upper steps (e.g., Figure 1). A turbulent boundary layer develops and free-surface aeration takes place when the outer edge of the boundary layer reaches the free-surface (Figure 1). Downstream significant aeration takes place and the flow is strongly turbulent.

Dimensionless void fraction distributions measured downstream of the inception point of free-surface aeration are presented in Figure 3. The black diamonds are single-tip probe data, and the squares are double-tip probe data: Grey squares for leading tip data and white square for trailing tip data. The results show a rapid flow aeration in the downstream flow direction (Figure 3).

In a transition flow regime (exp. 3), the void fraction distributions have a flat shape indicating as strong aeration of the entire cross-section (Figure 3A). At one step (i.e., step edge 6), the mean void fraction C_{mean} is about 76%, where the depth-average void fraction C_{mean} is defined as:

$$C_{mean} = \frac{1}{Y_{90}} \int_0^{Y_{90}} C dy, \tag{4}$$

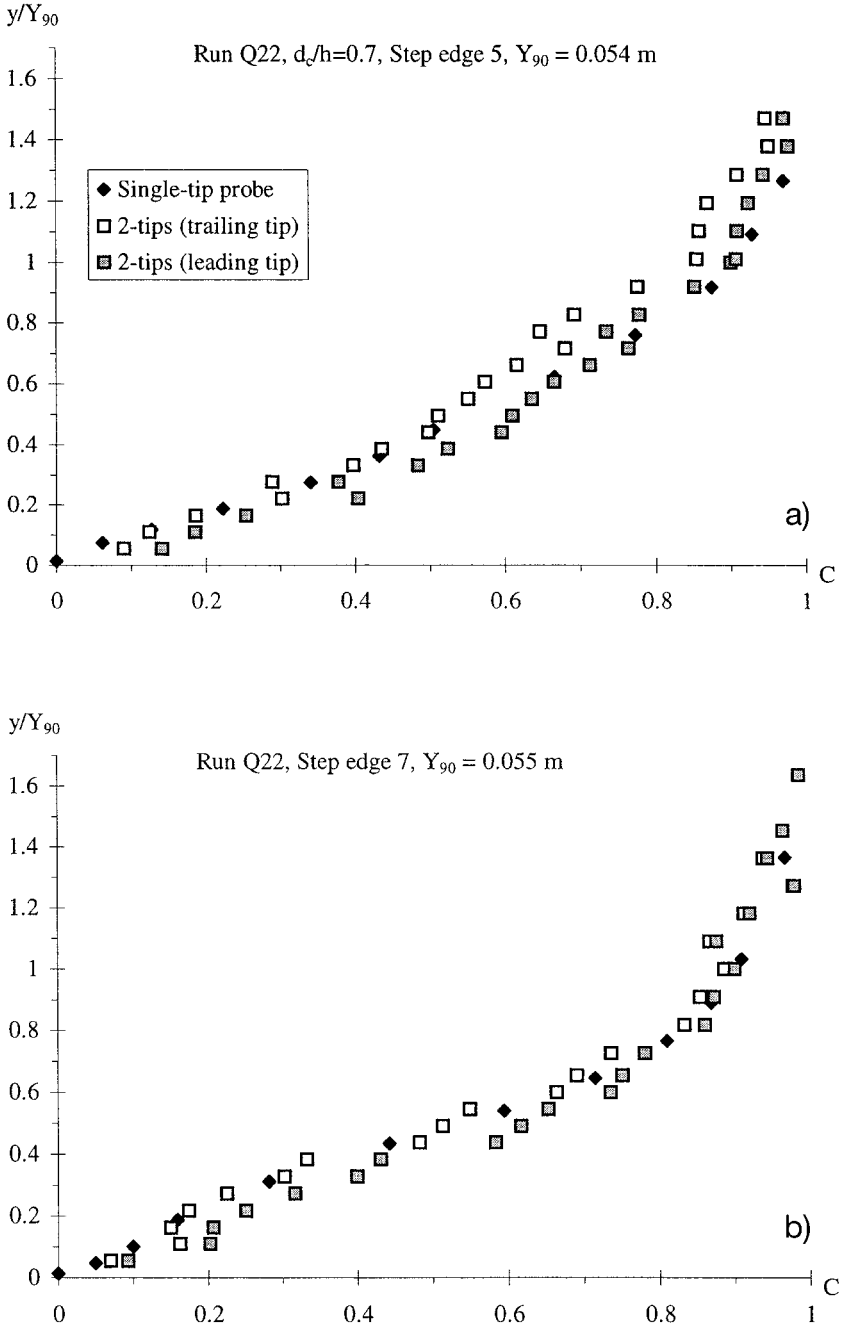

Figure 3. Dimensionless void fraction distributions. Black diamonds: Single-tip probe; grey rectangles: Leading tip of double-tip probe; white rectangles: Trailing tip of double-tip probe; dashed line: Equation (5). (a) Transition flow (Exp. No. 3). (b) Skimming flow (Exp. No. 2).

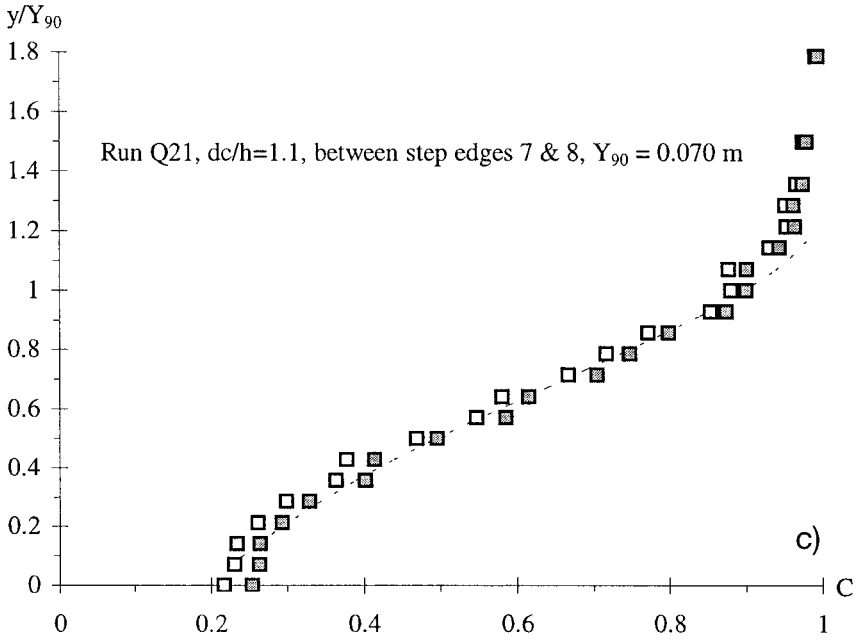

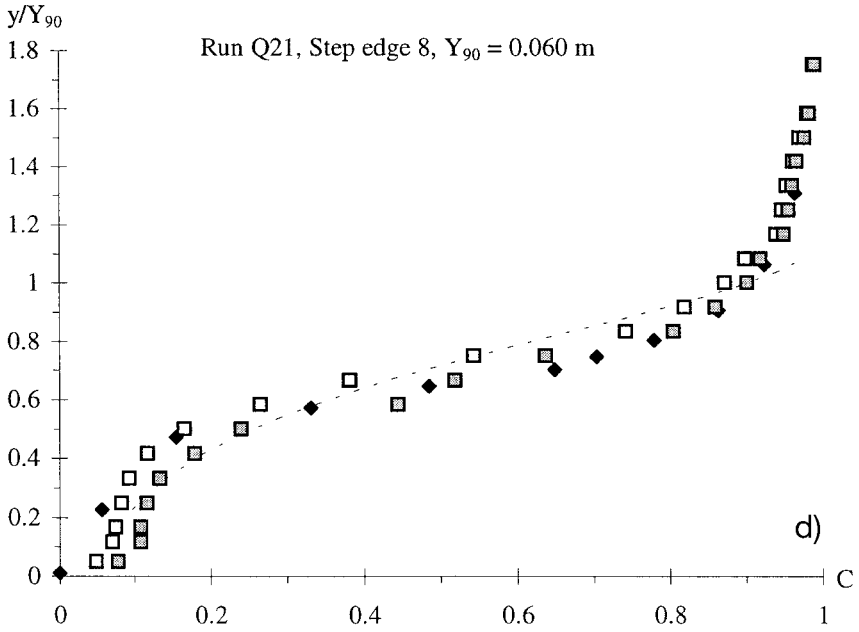

Figure 3. Continued.

y is the distance normal to the pseudo-bottom formed by the step edges, and Y_{90} is the location where $C = 0.9$. Visually the flow at step edge 6 was almost a deflected nappe 'bypassing' the step (Figure 1c).

In skimming flow, the data compare favourably with an advective diffusion model developed for smooth-invert chute flows:

$$C = 1 - \tanh^2\left(K' - \frac{y}{2D'\,Y_{90}}\right), \tag{5}$$

where tanh is the hyperbolic tangent function. D', a dimensionless turbulent diffusivity, and K', an integration constant, are functions of the mean air content C_{mean} only.[4] Equation (5) is shown in Figure 3b.

4. Discussion

In a transition flow, visual observations suggested that the flow was very chaotic from one step to the next one. A dominant flow feature was nappe stagnation on the horizontal step face associated with downstream spray. To an observer standing on the bank, the succession of stagnation points and downstream splashing gave a chaotic appearance to the flow. Splashing was observed to reach heights[5] in excess of five to seven times the step height.

In skimming flow, significant differences are observed between measurements at step edges and at half-distance between step edges. For all investigated flow conditions, greater mean air contents were measured in the lower flow region ($y/Y_{90} < 0.3$) between step edges than at the adjacent step edges. Flow visualisations demonstrated that the recirculating flow was highly aerated and that there were irregular fluid ejections from the cavity into the main stream, the process being sequential from upstream to downstream. The cavity flow was characterised by large vortical structures and it is suggested that bubbles were trapped in vortices by a kinematic mechanism. In an ideal horizontal vortex, a bubble is trapped within the vortex by centrifugal effect.[6] On a stepped chute, air bubbles may be entrapped into a recirculation vortex during its formation. Note that, during the study, three-dimensional cavity vortices were observed with typically four recirculating cells in the cross-wise direction.

[4]The relationship between D' and C_{mean} may be correlated as: $D' = (0.848C_{mean} - 0.00302)/(1 + 1.1375C_{mean} - 2.2925C_{mean}$, $C_{mean} < 0.07$, while the integration constant K' equals exactly: $K' = \tanh^{-1}(\sqrt{0.1}) + \frac{1}{2\,D'}$, where tanh is the hyperbolic tangent function [1, 13].

[5]Measured normal to the pseudo-bottom formed by the stepped edges.

[6]For an air bubble trapped in a vortex in the vertical plane in presence of a hydrostatic pressure gradient, the bubble spends most of the time in the downward moving fluid of the structure (e.g., [20, 21]).

5. Air-Water Velocity Distributions

Dimensionless air-water velocity data are presented in Figure 4. All the data were recorded with the double-tip resistivity probe. In a transition flow (exp. No. 3), major velocity redistributions were observed from step to step (Figure 4a).

In skimming flows, measurements performed at step edges show that, within the main body of the flow ($C < 90\%$), the velocity data compare favourably with a power law:

$$\frac{V}{V_{90}} = \left(\frac{y}{Y_{90}}\right)^{1/N}, \quad y/Y_{90} \leq 1, \tag{6a}$$

where V_{90} is the characteristic velocity at $y = Y_{90}$ and $N = 5.1$ and 6.1 for $d_c/h = 1.5$ and 1.1, respectively (Figure 4b). Although the velocity distribution in fully-developed open channel flows follows a logarithmic law, the writers believe that the power law approximation (Equation (6a)) is more consistent with the scatter of data and more practical for design purposes. The present results are consistent with the data of Boes [10, 22] measured at step edges in skimming flows on 30-deg and 50-deg stepped chutes. BOES' velocity data compare favourably with a 1/6 power law. In the splashing/spray region (i.e., $y > Y_{90}$), measurements conducted for void fractions of $0.9 < C < 0.98$ and $1 < y/Y_{90} < 1.8$ suggest that the air-water velocity distributions are nearly uniform:

$$\frac{V}{V_{90}} = 1, \quad y/Y_{90} \geq 1. \tag{6b}$$

Such a trend (i.e. Equation (6b)) indicates that most spray is little affected by air resistance. The result is consistent with the findings of Dodu [23] and Brattberg *et al.* [24] who investigated high-velocity water jets discharging into air.

In between step edges, skimming flow velocity profiles do not follow Equation (6) (Figure 4b). It is believed that the flow field is strongly affected by recirculation and momentum exchange between the main stream and the cavity flows.

For all three experiments (Table I), the air-water velocity distributions were integrated at each step edge. All the results satisfied the continuity equation for water within 12%:

$$\frac{Q_w}{W} = \int_0^{Y_{98}} (1 - C)V \, dy, \tag{7}$$

where Q_w is the measured water flow rate and W is the channel width. In skimming flows, the integration of the velocity distributions between step edges underestimated consistently the water flow rate by 10 to 20%, suggesting a positive net mass flux in the triangular cavity region.

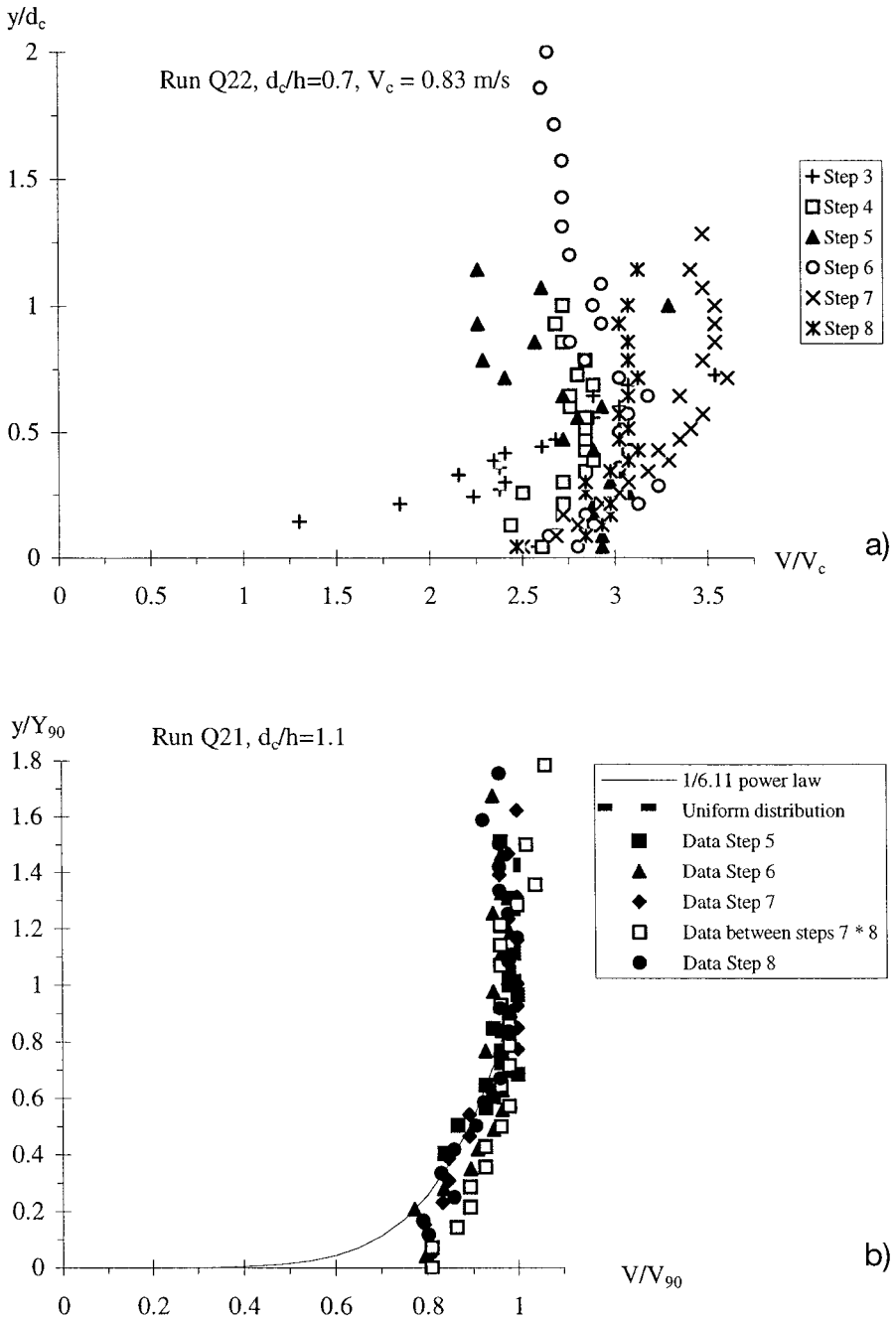

Figure 4. Dimensionless velocity distributions. (a) Transition flow (Exp. No. 3). (+) step edge 3, (white squares) step edge 4, (black triangles) step edge 5, (○) step edge 6, (×) step edge 7, (*) step edge 8. (b) Skimming flow (Exp. No. 2).

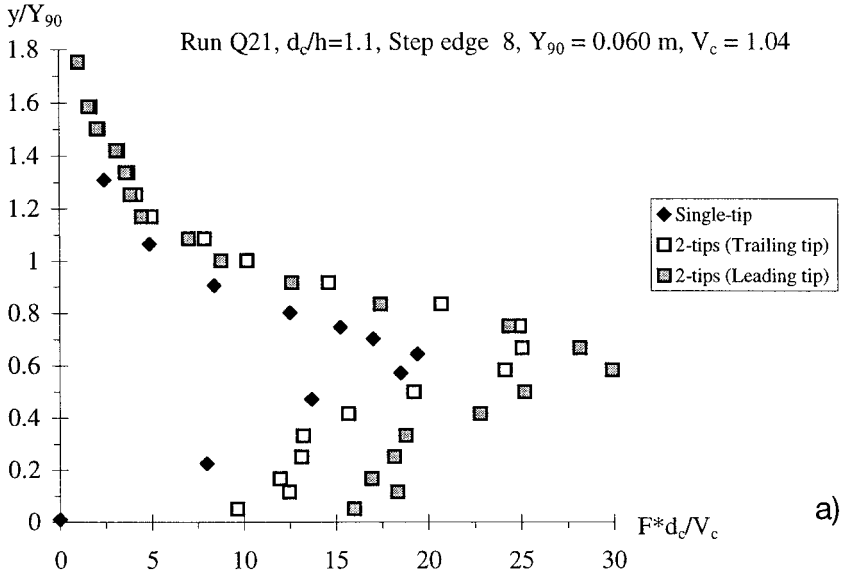

Figure 5. Dimensionless bubble count rate distributions. (a) Bubble count rate versus distance normal to the flow direction. Black diamonds: Single-tip probe; gray rectangles: Leading tip of double-tip probe; white rectangles: Trailing tip of double-tip probe. (b) Bubble count rate versus void fraction – Comparison with a parabolic law (Equation (8)).
(b1): Exp. No. 1 at step edge 8, $Y_{90} = 0.046$ m, $F_{max} = 240$ Hz.
(b2): Exp. No. 3 at step edge 8, $Y_{90} = 0.088$ m, $F_{max} = 132$ Hz.

6. Distributions of Bubble Count Rate and Air-Water Interface Area

The bubble count rate is a simple measure of the two-phase flow structure: i.e., it is inversely proportional to the mean bubble size for a given void fraction and air-water velocity. Typical distributions of dimensionless bubble count rate $F\ d_c/V_c$ are presented in Figure 5, where d_c and V_c are the critical flow depth and velocity respectively. In Figure 5b, the dimensionless bubble count rate is plotted as a function of the measured void fraction. The data are compared with a parabolic law:

$$\frac{F}{F_{max}} = 4C(1 - C), \tag{8}$$

where F_{max} is the maximum bubble count rate usually observed for $C = 0.5$. Such a parabolic shape was observed in smooth-chute flows, in high-velocity water jets and in hydraulic jumps [24–26].

The experimental data showed consistently larger measured count rates with the double-tip probe than with the single-tip probe. This suggests the existence of small bubbles with sizes ranging from 0.05 to 0.35 mm. In the spray/splashing region (i.e., $C > 0.8$ to 0.85), single-tip and double-tip probe data were nearly equal implying that most water droplets were larger than 0.35 mm. The results showed further that the maximum bubble count rate increased in the flow direction

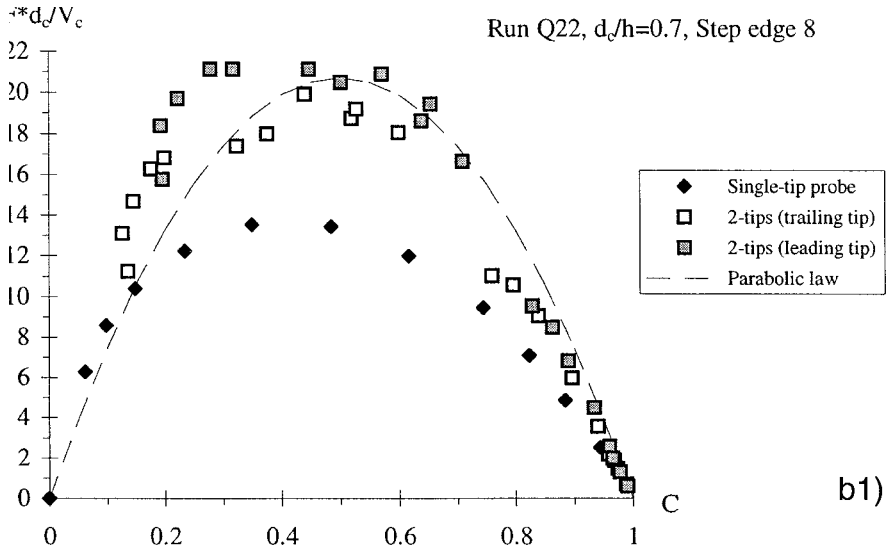

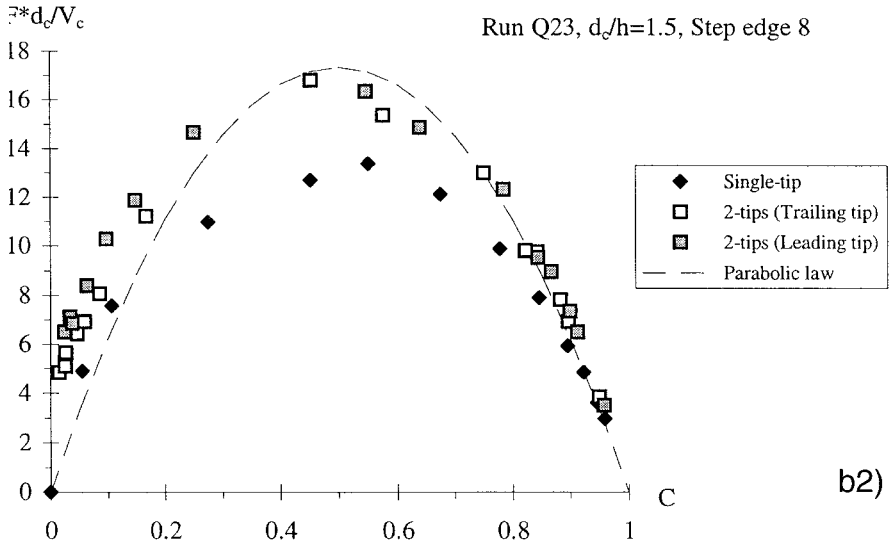

Figure 5. Continued.

for a given flow rate and probe (Figure 6). Figure 6 presents the longitudinal distributions of mean air content C_{mean} and dimensionless maximum bubble frequency $F_{max}d_c/V_c$ for experiment 2. The trend, illustrated in Figure 6, is characteristic of a longitudinal increase in mean void fraction and the presence of finer bubbles as a result of bubble breakup by turbulent shear.

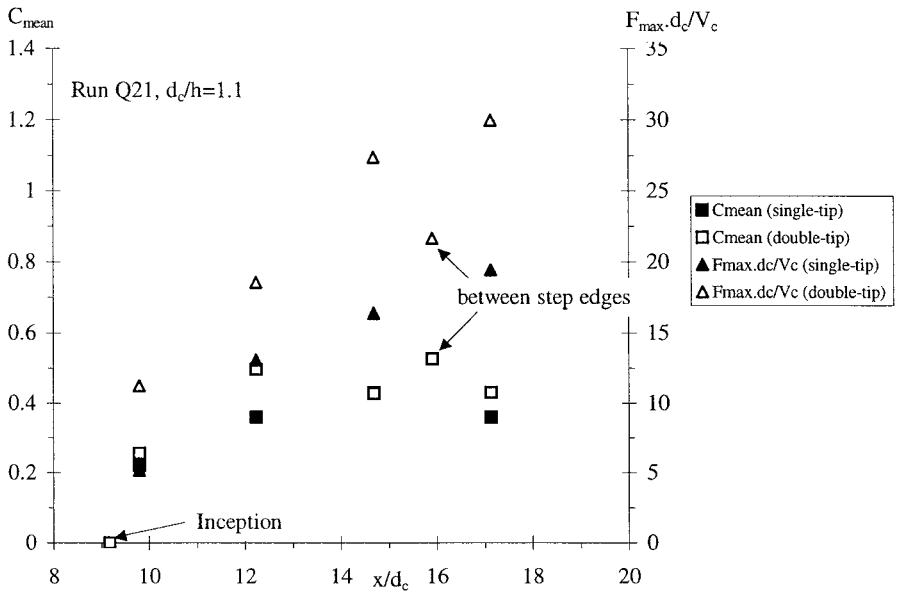

Figure 6. Longitudinal distributions of mean air content and dimensionless maximum bubble frequency.
Experiment 2, $q_w = 0.114$ m^2 s^{-1}.

These reasonings are consistent with measured chord length size distributions (Figure 7). In Figure 7, each graph presents the normalised chord length probability distribution function where the histogram columns represent the probability of a bubble chord length in 0.5 mm intervals: e.g., the probability of a chord length from 2.0 to 2.5 mm is represented by the column labelled 2.0. The last column (i.e., > 20) indicates the probability of bubble chord lengths larger than 20 mm. Air bubble chord length distributions are in white and water droplet chord length distributions are in black. The data give some information on the characteristic sizes of air bubbles and water droplets. They show the broad spectrum of bubble and droplet chord lengths observed at each location: i.e., from less than 0.5 mm to larger than 20 mm (Figure 7). Results from both the bubbly flow region ($C < 0.3$ to 0.4) and the splashing region (0.6 to 0.8 $< C$) are shown.

The air bubble chord length distributions are skewed with a preponderance of small bubble sizes relative to the mean. The probability of bubble chord lengths is the largest for bubble sizes between 0 and 1.5 mm for $C \approx 0.1$ and between 0 and 2.5 mm for $C \approx 0.2$. It is worth noting the large amount of bubbles larger than 20 mm for $C \approx 0.2$. These might be large air packets surrounding water structures.

Although water droplet chord length distributions appeared skewed with a preponderance of small drop sizes relative to the mean, the distributions differ from bubble chord length distributions for similar liquid and void fractions respectively, indicating consistently larger droplet chord lengths (Figure 7). A similar result was noted in smooth-invert chute flow [27].

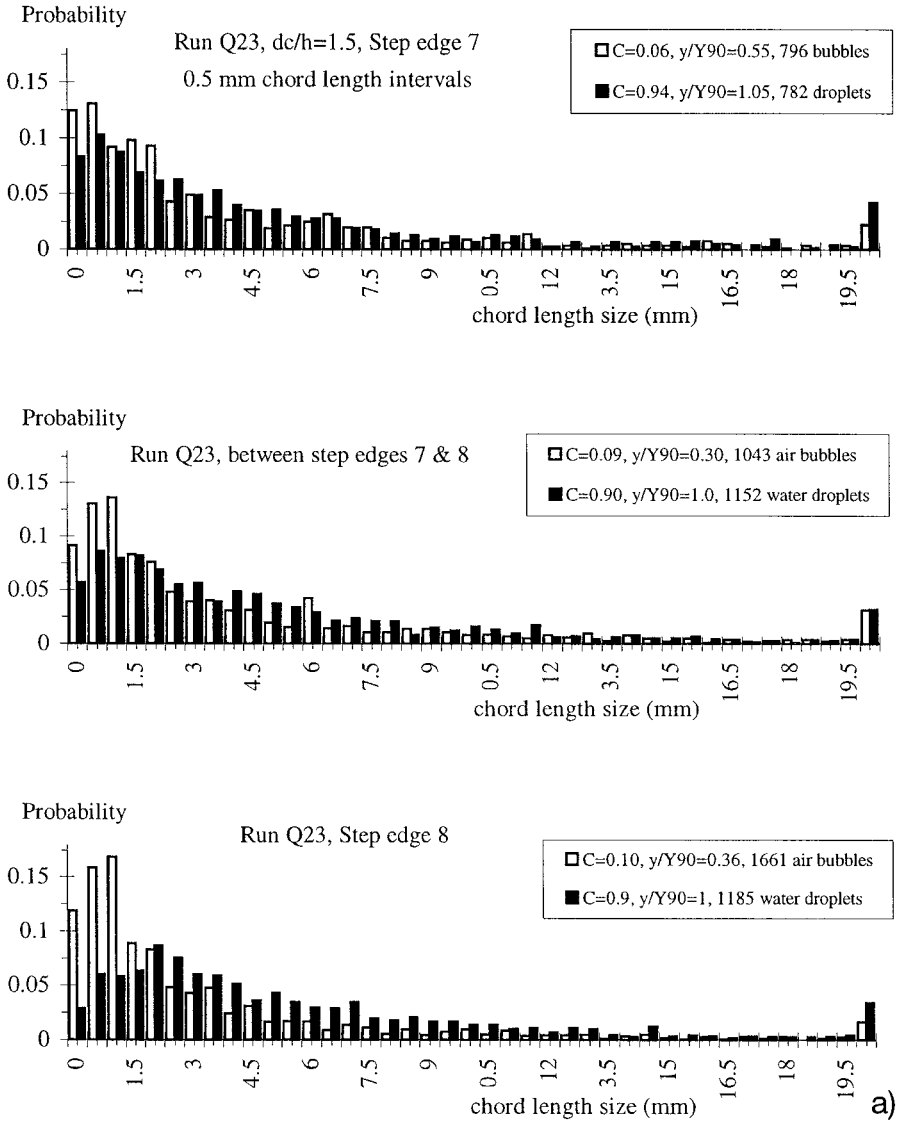

Figure 7. Bubble and droplet chord length distributions (white = air bubbles – black = water droplets).
(a) Void and liquid fractions: 10% (Exp. No. 1).
(b) Void and liquid fractions: 20% (Exp. No. 2).

Dimensionless specific interface area distributions are presented in Figure 8. Double-tip probe data were computed as Equation (3). For the single tip probe, the

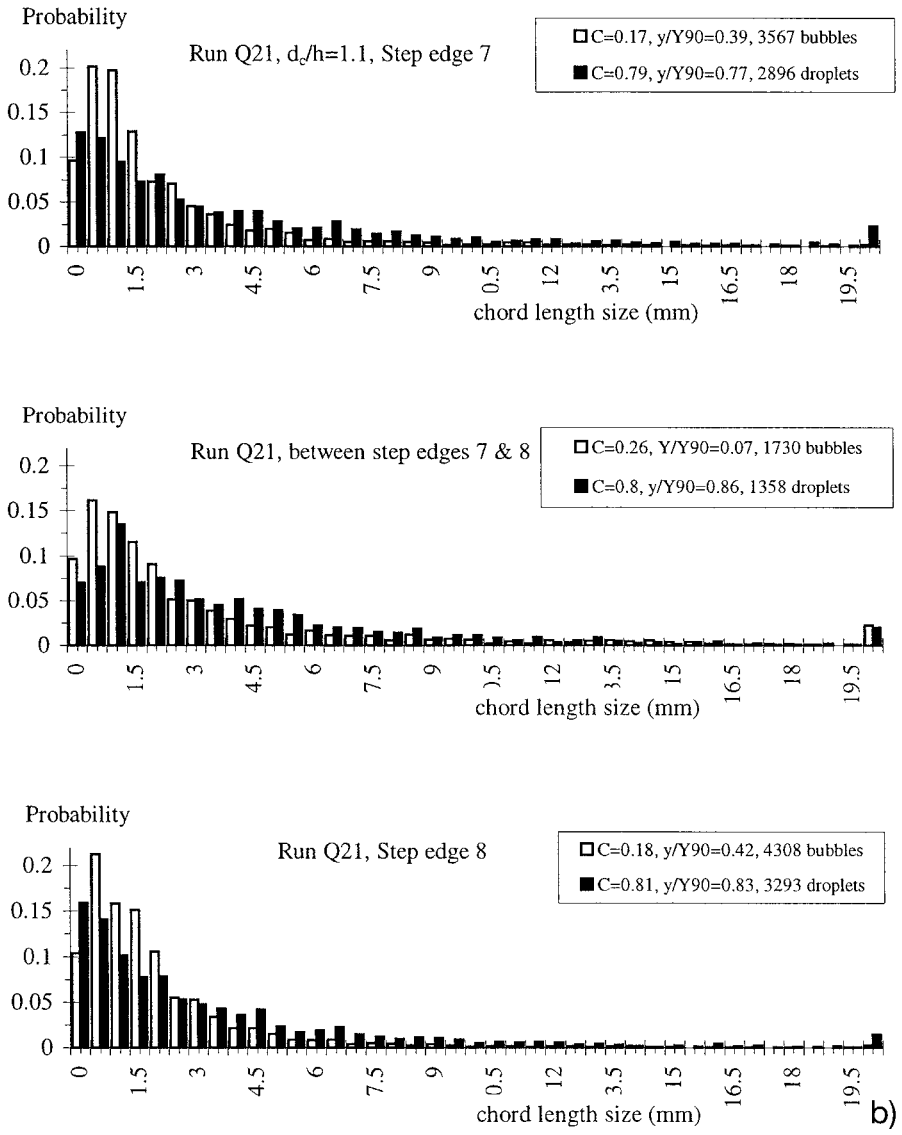

Figure 7. Continued.

specific interface area was estimated from the measured bubble count rate and the mean flow velocity:

$$a \approx 4\frac{F}{q_w}\int_0^{Y_{90}} (1 - C)\, dy \text{ single-tip probe,} \tag{9}$$

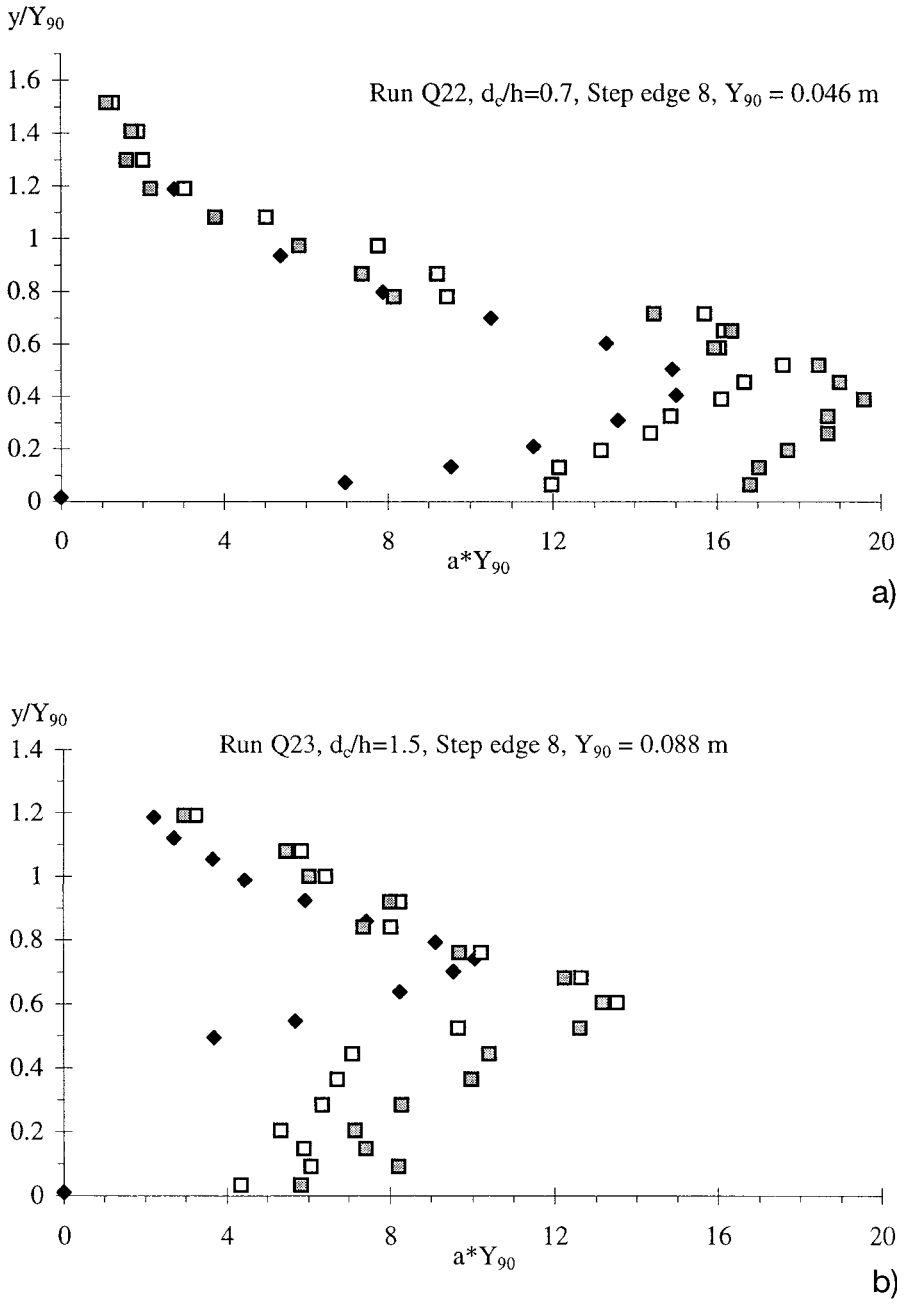

Figure 8. Distributions of dimensionless specific interface area a^*Y_{90}. Black diamonds: Single-tip probe; white rectangles: Trailing tip of double-tip probe; gray rectangles: Leading tip of double-tip probe.
(a) Transition flow (Exp. No. 3).
(b) Skimming flow (Exp. No. 1).

where q_w is the water discharge per unit width. Experimental results (Figure 8) showed maximum specific interface areas up to 650 m^{-1},[7] with depth-average mean specific area ranging from 20 to 310 m^{-1}.

For all the skimming flow experiments, greater specific interface areas were measured in between step edges than at the adjacent step edges. It is believed that the aeration of the recirculation flow contributes even further to the interface area.[8]

7. Discussion

During the present study, void fraction data were nearly independent of the probe type. Flow visualisations showed a preponderance of millimetric size bubbles. As the void fraction derives primarily from the cumulative contribution of large bubbles, the sensor size had little effect on the void fraction data because the probe sensor sizes were smaller than the characteristic bubble size. Bubble count data highlighted greater bubble count detection with the smaller sensor size (2-tips probe), indicating the existence of fine air-water structures with sizes below 0.35 mm. Comparisons between specific interface area measurements indicate consistently that the single-tip probe provides conservative estimate of the same order of magnitude as the double-tip resistivity probe, although only one sensor is used. The results suggest that, if the water discharge is known, the simple single-tip probe could be used to measure the air-water interface area and hence to predict the aeration efficiency of the system. The latter may be deduced from the basic mass transfer law. For volatile chemicals (e.g., oxygen in water), the mass transfer equation at steady state yields:

$$\frac{\partial}{\partial_x} C_{\text{gas}} = \frac{k_L a}{V} (C_s - C_{\text{gas}}), \tag{10}$$

where C_{gas} is the concentration of the dissolved chemical in liquid, x is the distance in the flow direction, C_s is the concentration of dissolved gas in water at equilibrium and K_L is the liquid film coefficient. Kawase and Moo-Young [28] showed that the mass transfer coefficient K_L is almost constant regardless of bubble sizes and flow situations. The integration of Equation (10) using measured specific interface areas may provide an estimate of the mass transfer rate. A comparison between single-tip and double-tip resistivity probe data is presented in Figure 9. Figure 9 shows the aeration efficiency in terms of dissolved oxygen at 20 °C, standard pressure and zero salinity. The results highlight the close prediction achievable with the sturdy single-tip probe.

[7] That is, nearly twice the surface area of a basketball court in one cubic metre of air and water.

[8] No measurement was conducted in the recirculation cavity ($y < 0$) to avoid probe tip damage. Matos *et al.* [29] presented additional air-water data measured above the recirculation cavity.

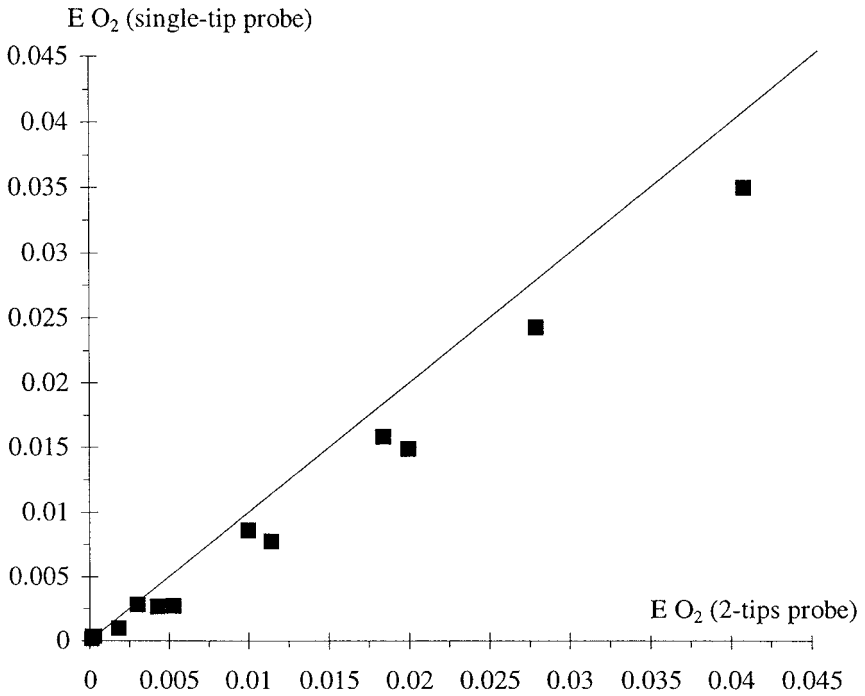

Figure 9. Estimated aeration efficiency in terms of oxygen at 20 °C and standard pressure. Comparison between double-tip and single-tip results (Experiments 1, 2 and 3).

7.1. COMPARISON BETWEEN LEADING AND TRAILING TIP SIGNALS

With the double-tip resistivity probe, the analysis of the leading and trailing tip signals yielded close results in terms of void fraction and bubble count rate distributions (hence specific interface area). The agreement suggests that, for this probe design (Figure 2), the trailing tip is little affected by the leading tip support in this type of flow conditions. The agreement between the two signal results was initially surprising, as some degree of interference from the leading tip might be expected. Further detailed comparisons confirmed the finding.

8. Conclusion

The air-water flow properties down a stepped cascade were measured with resistivity probes. Detailed interfacial properties were recorded with both single-tip and double-tip probes (Figures 3–8). The results emphasise the air-water gas transfer potential of a stepped cascade with large measured air-water interface areas: e.g., mean air contents up to 76%, maximum bubble count rates over 280 Hz, depth-averaged air-water specific areas up to 310 m^{-1}. A comparison between single-tip and double-tip resistivity probe results shows that the simple robust single-tip probe can provide sound, although conservative gas-liquid interfacial properties

and accurate aeration efficiency. Such a simple measurement technique with robust outputs is a more appropriate device for use in the field and in industrial plants. It must be noted that the water flow rate must be known when using a single-tip probe to estimate interfacial properties.

Future work is however needed to compare aeration efficiencies estimated with detailed interfacial area data and based upon dissolved gas measurements.

Acknowledgements

The writers acknowledge the assistance of G. Illidge, M. Eastman and N. Van Schagen (Brisbane, Australia).

References

1. Chanson, H.: 1997, *Air Bubble Entrainment in Free-Surface Turbulent Shear Flows*, Academic Press, London, U.K., 401 p.
2. Robison, R.: 1994, Chicago's Waterfalls, *Civil Engineering, ASCE* **64**, 36–39.
3. Gosse, P. and Gregoire, A.: 1997, Dispositif de réoxygénation artificielle du sinnamary à l'aval du barrage de Petit-Saut (Guyane) (Artificial re-oxygenation of the sinnamary, downstream of Petit-Saut dam (French Guyana)), *Hydroécol. Appl.* **9**, 23–56 (in French).
4. Hoek, J.P. van der, Kappelhof, J.W.N.M. and Hijnen, W.A.M.: 1992, Biological nitrate removal from ground water by sulphur/limestone denitrification, *J. Chem. Tech. Biotechnol.* **54**, 197–200.
5. Chanson, H.: 1995a, *Hydraulic Design of Stepped Cascades, Channels, Weirs and Spillways*, Pergamon, Oxford, U.K., January, 292 p.
6. Jones, O.C. and Delhaye, J.M.: 1976, Transient and statistical measurement techniques for two-phase flows: A critical review, *Int. J. Multiphase Flow* **3**, 89–116.
7. Cartellier, A. and Achard, J.L.: 1991, Local phase detection probes in fluid/fluid two-phase flows, *Rev. Sci. Instrum.* **62**, 279–303.
8. Bachalo, W.D.: 1994, Experimental methods in multiphase flows, *Int. J. Multiphase Flow* **20**, 261–295.
9. Ruff, J.F. and Frizell, K.H.: 1994, Air concentration measurements in highly-turbulent flow on a steeply-sloping chute, In: *Proceedings of the Hydraulic Engineering Conference, ASCE*, Vol. 2, pp. 999–1003, Buffalo, U.S.A.
10. Boes, R.M.: 2000a, Scale effects in modelling two-phase stepped spillway flow. In: H.E. Minor and W.H. Hager (eds.), *International Workshop on Hydraulics of Stepped Spillways*, Balkema Publ., Zürich, Switzerland, pp. 53–60.
11. Bos, M.G.: 1976, *Discharge Measurement Structures*, Publication No. 161, Delft Hydraulic Laboratory, Delft, The Netherlands (also Publication No. 20, ILRI, Wageningen, The Netherlands).
12. Ackers, P., White, W.R., Perkins, J.A. and Harrison, A.J.M.: 1978, *Weirs and Flumes for Flow Measurement*, John Wiley, Chichester, U.K., 327 pp.
13. Chanson, H.: 1995b, *Air Bubble Entrainment in Free-Surface Turbulent Flows. Experimental Investigations*, Report CH46/95, Department of Civil Engineering, University of Queensland, Australia, June, 368 p.
14. Cummings, P.D. and Chanson, H.: 1997, Air entrainment in the developing flow region of plunging jets. Part 2: Experimental, *J. Fluids Eng., Trans. ASME* **119**, 603–608.
15. Sene, K.J.: 1984, *Aspects of Bubbly Two-Phase Flow*, Ph.D. Thesis, Trinity College, Cambridge, U.K.

16. Chanson, H.: 1988, *A Study of Air Entrainment and Aeration Devices on a Spillway Model*, Ph.D. Thesis, Ref. 88-8, Department of Civil Engineering, University of Canterbury, New Zealand.
17. Chanson, H. and Toombes, L.: 2001, *Experimental Investigations of Air Entrainment in Transition and Skimming Flows down a Stepped Chute. Application to Embankment Overflow Stepped Spillways*, Research Report CE 158, Department of Civil Engineering, The University of Queensland, Brisbane, Australia.
18. Clark, N.N. and Turton, R.: 1988, Chord length distributions related to bubble size distributions in multiphase flows, *Int. J. Multiphase Flow* **14**, 413–424.
19. Moursali, E., Marie, J.L. and Bataille, J.: 1995, An upward turbulent bubbly boundary layer along a vertical flat plate, *Int. J. Multiphase Flow* **21**, 107–117.
20. Tooby, P.F., Wick, G.L. and Isaacs, J.D.: 1977, The motion of a small sphere in a rotating velocity field: a possible mechanism for suspending particles in turbulence, *J. Geophys. Res.* **82**, 2096–2100.
21. Nielsen, P.: 1992, Coastal bottom boundary layers and sediment transport, *Adv. Ser. Ocean Eng.* **4**, World Scientific Publ., Singapore.
22. Boes, R.M.: 2000b, *Zweiphasenstroömung und Energieumsetzung auf Grosskaskaden. (Two-Phase Flow and Energy Dissipation on Cascades.)*, Ph.D. Thesis, VAW-ETH, Zürich, Switzerland (in German).
23. Dodu, J.: 1957, Etude de la couche limite d'air autour d'un jet d'eau à grande vitesse. ('Study of the boundary layer around a high velocity water jet.'), In: *Proceedings of the 7th IAHR Congress*, Lisbon, Portugal, paper D6 (in French).
24. Brattberg, T., Chanson, H. and Toombes, L.: 1998, Experimental investigations of free-surface aeration in the developing flow of two-dimensional water jets, *J. Fluids Eng. Trans. ASME* **120**, 738–744.
25. Chanson, H.: 1997b, Air bubble entrainment in open channels. Flow structure and bubble size distributions, *Int. J. Multiphase Flow* **23**, 193–203.
26. Chanson, H. and Brattberg, T.: 2000, Experimental study of the air-water shear flow in a hydraulic jump, *Int. J. Multiphase Flow* **26**, 583–607.
27. Chanson, H.: 1999, Turbulent open-channel flows: Drop-generation and self-aeration. Discussion, *J. Hyd. Engrg., ASCE* **125**, 668–670.
28. Kawase, Y. and Moo-Young, M.: 1992, Correlations for liquid-phase mass transfer coefficients in bubble column reactors with Newtonian and non-Newtonian fluids, *Can. J. Chem. Eng.* **70**, 48–54.
29. Matos, J., Yasuda, Y. and Chanson, H: 2001, Interaction between free-surface aeration and cavity recirculation in skimming flows down stepped chutes, In: *Proceedings of the 29th IAHR Congress*, Beijing, China, Theme D, Vol. 2, Tsinghua University Press, Beijing, G. LI Ed., pp. 611-617. (CD-ROM, Tsinghua University Press, ISBN 7-900637-10-9.)